JOURNAL OF THERMOPHYSICS AND HEAT TRANSFER
Vol. 25, No. 1, January–March 2011

Flow and Heat Transfer in Hydraulic Reservoir of Thrust Vector Control System

D. T. Frate,* N. T. Pham,* R. J. Christie,† J. B. Mcquillen,‡ B. J. Motil,§ and D. F. Chao‡
NASA John H. Glenn Research Center at Lewis Field, Cleveland, Ohio 44135
and
N. Zhang¶
Ohio Aerospace Institute, Cleveland, Ohio 44142

DOI: 10.2514/1.51163

Launch vehicle thrust vector control provides vehicle steering functions during powered flight starting from liftoff until engine cutoff. The thrust vector control on the first stage of Ares 1 provides steering during the first 133 s of ascent, while the thrust vector control on the upper stage provides steering for the next 465 s. Heat absorption by the hydraulic reservoir is a key factor in the performance of the upper stage thrust vector control system. A computational fluid dynamics simulation of the fluid flow and heat transfer in the hydraulic reservoir in the Ares 1 upper stage thrust vector control has been performed with the corresponding operating conditions and environmental conditions. The reservoir was set at 75% full of working fluid. Two steady-state cases, for fluid inlet temperatures of 294.3 and 394.3 K, and one transient case for the fluid inlet temperature ramping from 294.3 to 352.2 K over a 4.63 min period were simulated. The temperature, velocity, and pressure fields, as well as the absorbed heat for each case, were obtained, which have improved the understanding of the thermal dynamics of the thrust vector control subsystem.

Nomenclature

A, B, C, D	=	strategic positions in the reservoir shown in Fig. 1
a, b, c, d	=	strategic sections of the reservoir shown in Fig. 1
C_h	=	constant in Eq. (9)
C_{pa}	=	specific heat at constant pressure of the cooling air, J/kg K
C_{pf}	=	specific heat at constant pressure of the working fluid, J/kg K
D	=	diameter of cylindrical body, m
dt	=	time step, s
h	=	specific enthalpy of the working fluid, J/kg
$\bar{h}_c$	=	average heat transfer coefficient, W/m^2 K
$h_{f,\text{in}}$	=	fluid-specific enthalpy at the inlet of the inlet tube in the transient process, J/kg
$h_{f,\text{out}}$	=	fluid-specific enthalpy at the outlet of the outlet tube in the transient process, J/kg
$h_{f,\text{out},1}$	=	fluid-specific enthalpy at the outlet of the outlet tube during $0 \sim 8$ s, J/kg
$h_{f,\text{out},2}$	=	fluid-specific enthalpy at the outlet of the outlet tube during $8 \sim 90$ s, J/kg
$h_{f,\text{out},3}$	=	fluid-specific enthalpy at the outlet of the outlet tube during $90 \sim 278$ s, J/kg
k_a	=	thermal conductivity of the cooling air, W/m K
k_f	=	thermal conductivity of the working fluid, W/m K
m, n	=	constants in Eq. (9)
$\dot{m}$	=	mass flow rate of the working fluid, kg/s
Pr	=	Prandtl number
Pr_s	=	Prandtl number evaluated at the wall temperature
t	=	time, s
U_∞	=	air velocity to pass over the cylindrical body, m/s
ΔH	=	total absorbed heat by the reservoir during the transient process, kJ
μ_f	=	absolute viscosity of the working fluid, N s/m^2
μ_α	=	absolute viscosity of the cooling air, N s/m^2
ρ_a	=	density of the cooling air, kg/m^3
ρ_f	=	density of the working fluid, kg/m^3

Received 14 June 2010; revision received 9 August 2010; accepted for publication 12 August 2010.

*Aerospace Engineer, Launch System Project Office, Mail Stop 77-7.
†Aerospace Engineer, Thermal Systems Branch, Mail Stop 86-12.
‡Research Aerospace Engineer, Fluid Physics and Transport Branch, Mail Stop 77-5.
§Supervisory Aerospace Engineer, Fluid Physics and Transport Branch, Mail Stop 77-5.
¶Senior Scientist, Workforce Enhancement; currently at Fluid Physics and Transport Branch, Mail Stop 77-5 (Corresponding Author).

I. Introduction

NASA is developing the Ares 1 rocket to serve as the new space transportation system under the Constellation Program, which would carry the Orion spacecraft and its crew on missions to the International Space Station and then later on to the moon and beyond [1].

The upper stage (US) thrust vector control (TVC) system for the Ares 1 rocket is a critical aspect of the flight to deliver the Orion capsule into Low Earth Orbit. During first stage operation, the US TVC system holds the US engine still preventing damage. During US flight, the TVC system working in conjunction with the guidance, navigation and control system, moves the US engine, redirecting the thrust to keep the vehicle on the proper flight trajectory [2]. An initial prototype of Ares 1 US TVC hydraulic system was developed by the NASA Glenn Research Center TVC team, and tested with a single actuator to characterize performance [3]. The TVC team has also built a full flightlike TVC system that is undergoing testing in 2010 which will support a key decision point leading to the Critical Design Review. The two hydraulic reservoirs are a key component of the TVC system, which is located on the US thrust cone, as shown in Fig. 2. The reservoirs provide hydraulic fluid volumes, hydraulic pump suction pressurization, and allow for fluid thermal expansion and heat load absorption. In view of the heat absorption by the hydraulic reservoir being a key factor in the performance of the TVC system, a computational fluid dynamics (CFD) simulation of the fluid flow and heat transfer in the hydraulic reservoir in the Ares 1 US TVC has been performed with the corresponding operating conditions and environmental conditions, which is beneficial to better

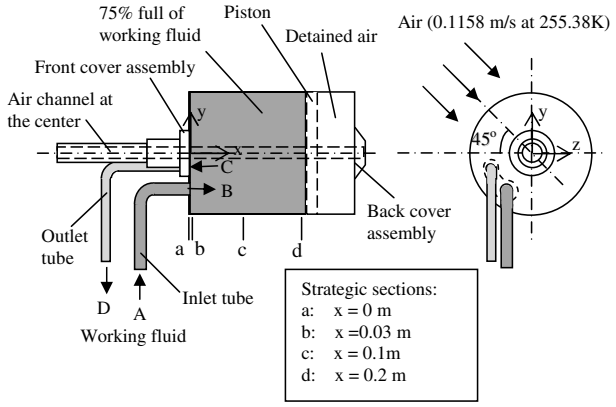

Fig. 1 Diagram of the working fluid flow in the reservoir and the air cooling route.

understand the TVC operational performance. Two steady-state cases and one transient case were conducted.

II. Work Conditions of the Reservoir and CFD Model

Although the hydraulic reservoir body geometry is very complicated, the flow routes of the working fluid in the reservoir and the air passing over it are simple, forming a conjugate heat transfer process. The working fluid, MIL-PRF-83282, is pumped into the reservoir via the inlet tube, which experiences cooling by air flow of temperature 255.38 K (0°F) at normal pressure. The air passes over the reservoir with velocity of 0.1158 m/s at 45° angle with the centerline. A diagram of the working fluid flow route in the reservoir and the air cooling route are shown in Fig. 1. Obviously, the working fluid is cooled by the air in the conjugate heat transfer process between them. As pointed out by Dorfman and Renner [4], the heat transfer coefficient is usually determined experimentally and no well-found theoretical approach was available until the last few decades. However, starting from the end of the 1960s, heat transfer problems began to be considered using a conjugate, coupled, or adjoint formulation, corresponding to the problems containing two or more subdomains with phenomena described by different differential equations. It is this advanced modeling of convective conjugate heat transfer problems that enables analytical solutions of many conjugate heat transfer problems can be obtained and paves the way for solving the complicated conjugate problems using numerical methods. More and more papers studying the conjugate heat transfer, including both relevant steady-state heat transfer [5–10] and transient heat transfer [11–15], have been published. A comprehensive review of conjugate problems in convective heat transfer has been made by Dorfman and Renner [4].

To conduct a CFD simulation of the fluid flows both for the working fluid in the reservoir and the cooling air around it, as well as the heat transfer between the working fluid and the cooling air, a geometric model had to be established first. The ACIS file for the reservoir has six bodies. Each one has a complicated geometry. When the STP file of the reservoir three-dimensional drawing was imported into GAMBIT 2.4.6, six volumes with 1015 faces were identified. Because the hydraulic reservoir is located at the thrust cone outer surface, as shown in Fig. 2, the air flows at a varying velocity from 0.0762 m/s at a distance of 0.831 m before the reservoir to 0.1524 m/s at 0.33 m after the reservoir, passing over the reservoir at 0.1158 m/s. To simulate the air flow condition a truncated elliptic cone was built up to create a channel for the air flow passing over the reservoir, as shown in Fig. 3. Considering the air detained in the solid body and the flowing air passing over the reservoir in the cone channel, two new separated volumes and three new faces were formed. The 1018 faces were reduced to only 75 faces through the *merge* operation in Gambit, and consequently, all the volumes, except the inlet tube and the outlet tube of the reservoir, were transferred to corresponding virtual volumes. Based on the virtual geometry of the model, the volumes were meshed to produce 2,829,650 cells with 6,388,196 facets. To run the CFD simulation, three-dimensional version of FLUENT 6.3.26 was used. The grid quality is checked by both GAMBIT and FLUENT, for example, if any grid skewness is higher than 0.9, GAMBIT would not allow creation of the mesh file which will be read by FLUENT for the case simulations. Even the grid quality is passed by GAMBIT. The first step of running FLUENT will check the grid again and sooth/swap the grids. Only qualified grids are accepted by FLUENT and allowed to run.

To obtain high numerical accuracy, a fine mesh was created by GAMBIT. The grid check showed that the minimum volume size was 8.318223×10^{-11} m^3 and the maximum volume size was 4.353452×10^{-5} m^3, while the minimum face area was 5.287424×10^{-7} m^2 and the maximum face area was 2.698065×10^{-3} m^2. The small size of the volumes and faces were created in fine parts of the reservoir and in the vicinity of the boundaries, and size functions were used to smooth the changes from the small sizes to the large sizes of the volumes and faces. When conducting the simulations using FLUENT, 3DD (double precision) version was chosen. For all

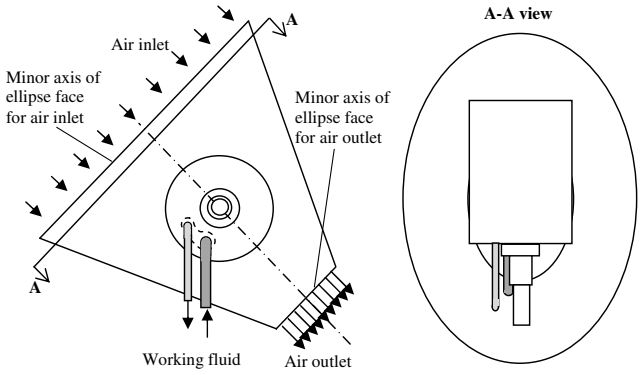

Fig. 3 Cooling air channel for simulation of the air flow passing over the reservoir.

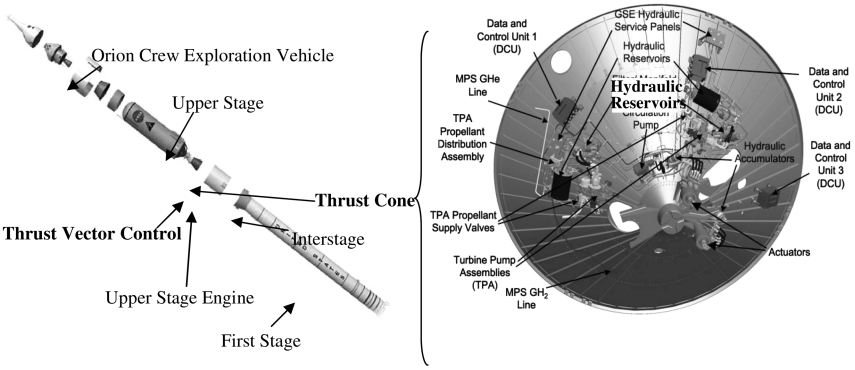

Fig. 2 Hydraulic reservoirs location on the thrust cone of Ares 1 US.

the cases of the simulations, the second order upwind discretizations for both momentum and energy, and PRESTO! discretization scheme for pressure were taken. The PISO pressure-velocity coupling was used and the following under-relaxation factors were set: 0.1 for pressure, 1 for density, body forces, and energy, and 0.4 for momentum. The following convergence criteria were taken: velocity residuals in all three directions are less than 10^{-3}; energy and continuity residuals are less than 10^{-6}.

The simulations of the flows and heat transfer for both steady-state cases and a transient case have been conducted. The two steady-state cases are for the working fluid inlet temperatures being 294.3 and 394.3 K, respectively, while the transient case is for inlet temperature of the working fluid ramping from 294.3 to 352.2 K over a 4.63 min period.

It should be noted that in all the cases both the working fluid flow and the cooling air flow were laminar. The thermophysical properties of MIL-PRF-83282 were cited from the Aerospace Hydraulic Fluids Physical Properties in SAE AIR1362 [16]. The relevant properties, such as density ρ_f, specific heat c_{pf}, thermal conductivity k_f, and viscosity μ_f, were arranged to the following formulas:

$$\rho_f = 1031.7 - 0.65T \tag{1}$$

$$c_{p_f} = 996.325 + 3.475T \tag{2}$$

$$k_f = 266.347 \times 10^{-3}\text{–}326.316 \times 10^{-6}T \tag{3}$$

$$\mu_f = 2.218469 - 0.016901T + 4.489564 \times 10^{-5}T^2 - 3.983979 \times 10^{-8}T^3 \tag{4}$$

where T is temperature in international system of units (K). The relevant thermophysical properties of air were cited from the handbook edited by Raznjevič [17], which were arranged as

$$\rho_a = 4.219732 - 1.921319 \times 10^{-2}T + 3.813859 \times 10^{-5}T^2 - 2.779753 \times 10^{-8}T^3 \tag{5}$$

$$c_{p_a} = 1097.336 - 0.6575T + 0.00125T^2 + 6.205243 \times 10^{-14}T^3 \tag{6}$$

$$k_a = 0.00459 + 7.0 \times 10^{-5}T \tag{7}$$

$$\mu_a = 1.199288 \times 10^{-4} - 1.091574 \times 10^{-6}T + 3.749625 \times 10^{-9}T^2 - 4.1250 \times 10^{-12}T^3 \tag{8}$$

Table 1 Temperature and pressure at strategic positions

Point	$\dot{m}$, kg/s	p_g, kPa	T, K
A	0.1166	448.159	294.3
B	0.1166	445.915	294.2
C	0.1166	444.782	294.1
D	0.1166	444.006	294.0

The solid body material is aluminum whose properties were taken as constants: density is 2719 kg/m^3, specific heat is 871 J/kg K, and thermal conductivity is 202.4 W/m K.

III. Simulation Results

To reveal the flowfields of both the working fluid in the reservoir and the cooling air passing over the reservoir and their effects on the heat transfer between them, and consequently, to understand the working condition of the reservoir at the steady states, two typical steady-state cases have been simulated.

A. Steady-State Case 1

The working fluid is pumped into the reservoir with a flow rate of 1.3880×10^{-4} m^3/s (2.2 GPM) at a pressure of 448.159 kPa (65PSIG) and a temperature of 294.3 K. The simulation results give the most interested parameters at the strategic positions showing in Fig. 1, such as the tube inlet (position A), the reservoir body inlet (position B), the reservoir body outlet (position C), and the tube outlet (position D), which are listed in Table 1. The average specific heat in the reservoir is 2018.43 J/kg-K, and accordingly, the total absorbed heat by the reservoir, including the inlet and outlet tubes, is 65.9 W. It is noted that the working fluid was greatly cooled in the inlet and outlet tubes. The reservoir body itself only absorbs 40.01 W of heat, accounting for 60.7% of the total absorbed heat. The heat transfer from the outer cylindrical lateral wall of the reservoir to the air is 28.6 W, whose surface heat flux distribution is shown in Fig. 4a, while the heat directly transferred from the working fluid to the inner cylindrical lateral wall of the reservoir is only 27.3 W, whose surface heat flux distribution is shown in Fig. 4b (the larger cylindrical surface on the left). The heat flux difference between the outer and inner cylindrical lateral surfaces of the reservoir is mainly created by the axial heat conduction of the solid body, including the piston and the lateral wall itself. More interestingly, different heat transfer directions in the detained air chamber were observed, whose inner cylindrical lateral surface is shown in Fig. 4b (the smaller cylindrical surface on the right). The detail of the heat flux distribution on this surface is shown in Fig. 4c, using a different gray scale. It can be seen that heat is transferred from the detained air to the reservoir wall in the top portion while from the reservoir wall to the detained air in the bottom portion. This particular phenomenon is formed from the combination of the complex heat conductions through the piston as well as the lateral wall and the convection at both inner and outer

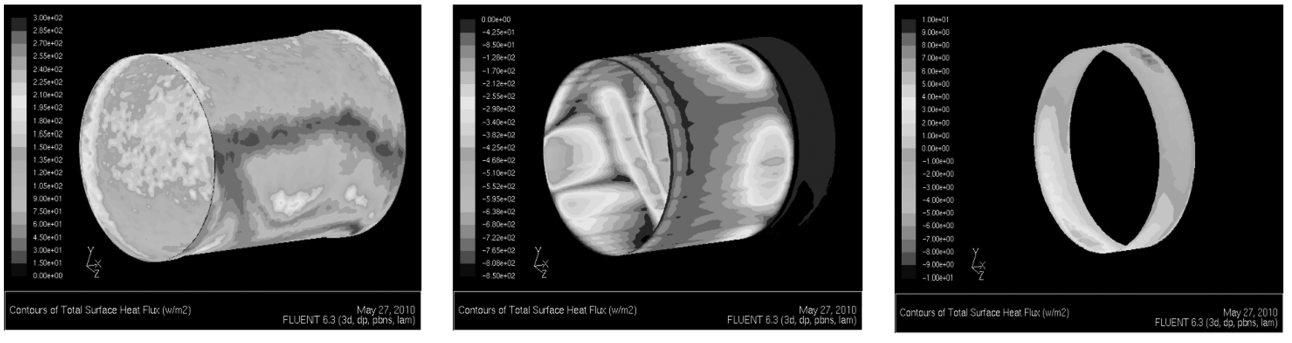

a) On outer cylinder lateral surface **b) On inner cylindrical lateral surface** **c) On inner cylindrical lateral surface with detained air**

Fig. 4 Surface heat fluxes on the cylindrical lateral surfaces.

surfaces of the cylinder wall, which can hardly be revealed by either calculations using empirical relations or experimental tests.

According to the simulation results, the heat transferred from the working fluid to the cooling air directly through the cylindrical lateral wall is only about 68.2% of the total heat absorbed by the reservoir body, while 31.8% of the heat is transferred to the cooling air through other paths, such as the front cover assembly, the back cover assembly, and the central air channel.

The air passing over the reservoir produced a wake of eddies after the reservoir, benefiting the heat transfer. It can be seen that the flow pattern, and consequently, the temperature distribution at various sections are different, as shown in Figs. 5a–5f, respectively. It should be explained that the section *a* crosses over the front cover assembly as shown in Fig. 1, in which the working fluid incoming-outgoing cabinet is located. The cross-sectional geometry of the incoming-outgoing cabinet is manifested by the lightest grayscale of the cylinder section in Fig. 5d, which indicates the highest temperature at this section. It is noted that the section average temperature increases with the distance from the entrance of the working fluid, and the air flow pattern changes, too.

As is well known, natural-convection heat transfer occurs whenever a body is placed in air at a lower temperature than that of the body. As a result of the temperature difference between the body and the air, the body heats the air and decreases the density of the air in the vicinity of the body surface. The difference in density of the air leads to downward flow of the heavier air and upward flow of the lighter air. The driving force of natural convection is the buoyant effect. It is the lower average temperature in the solid cover assembly that made less buoyant effect, as shown in Figs. 5a and 5d. Along with increase of the section average temperature, the buoyant effect is increased, and consequently, the wake of eddies of the cooling air flowing over the reservoir cylindrical wall is shifted up, as shown in Figs. 5d–5f.

Figure 6 shows the detail temperature distributions at the sections *a*, *b*, *c*, and *d* of the reservoir, including the air channel at the center shown in Fig. 1. The highest average temperature occurs in section *d*, which is near the piston. This occurs because the working fluid is shot straight onto the piston and spreads around the collision area that creates the stronger convection in the vicinity of the piston, and then produces the higher average temperature. It can be seen from Fig. 7a that the working fluid entrance jet at the inlet and the outflow stream at the outlet were formed, respectively, with the flow velocity larger than 0.03 m/s, while in the rest of the working fluid flow velocities were very small because the convection in the reservoir is very weak. It is the collision of the fluid with the piston plate that created the vortexes in the vicinity of the piston plate, as shown in Fig. 7b, and consequently, a higher average temperature in the vicinity of the piston was created and manifested itself in Fig. 6d, while the lower average temperatures occur at the other sections of the reservoir, see Figs. 6 and 8.

As mentioned above, the working fluid was not only cooled by the air passing round the cylindrical lateral wall but also by the air passing over the front cover assembly, the back cover assembly, and detained in the air chamber and the central channel of the reservoir. The variable heat fluxes at the different walls of the reservoir manifest themselves in the temperature fields of the air around the reservoir walls both inner and outer. Figure 8 shows the temperature distributions of the working fluid in the reservoir and the cooling air around the reservoir in the retained air chamber and the central channel at the section $z = 0$. It can be seen clearly that the maximum heat flux occurs on the cylindrical lateral wall for the thinnest thermal boundary while the least heat flux is in the middle of the central air channel where the highest temperature of air occurs due to the heat conduction without air convection there, and consequently, the least temperature gradient is formed.

In view of no experimental data available, an estimation of heat transfer for a cylinder in air cross flow was made. The Zukauakas correlation [18] was used to calculate the heat transfer coefficient:

$$\frac{\bar{h}_c D}{k_a} = C_h \left(\frac{U_\infty D \rho_a}{\mu_a}\right)^m Pr^n \left(\frac{Pr}{Pr_s}\right)^{0.25} \tag{9}$$

where $\bar{h}_c$ is the average heat transfer coefficient between the cylinder body and the cooling air, D is the diameter of the cylindrical body which was taken to be 0.23 m, equaling to the diameter of the reservoir cylindrical body, U_∞ is the air velocity to pass over the cylindrical body, which is 0.1158 m/s, Pr is the air Prandtl number evaluated at the bulk air temperature, Pr_s is air Prandtl number evaluated at the cylinder wall temperature, C_h, m, and n are the constants. Since the Reynolds number of the air crossing over the cylindrical body is about 2071 and $Pr \approx 0.71$, the constants should

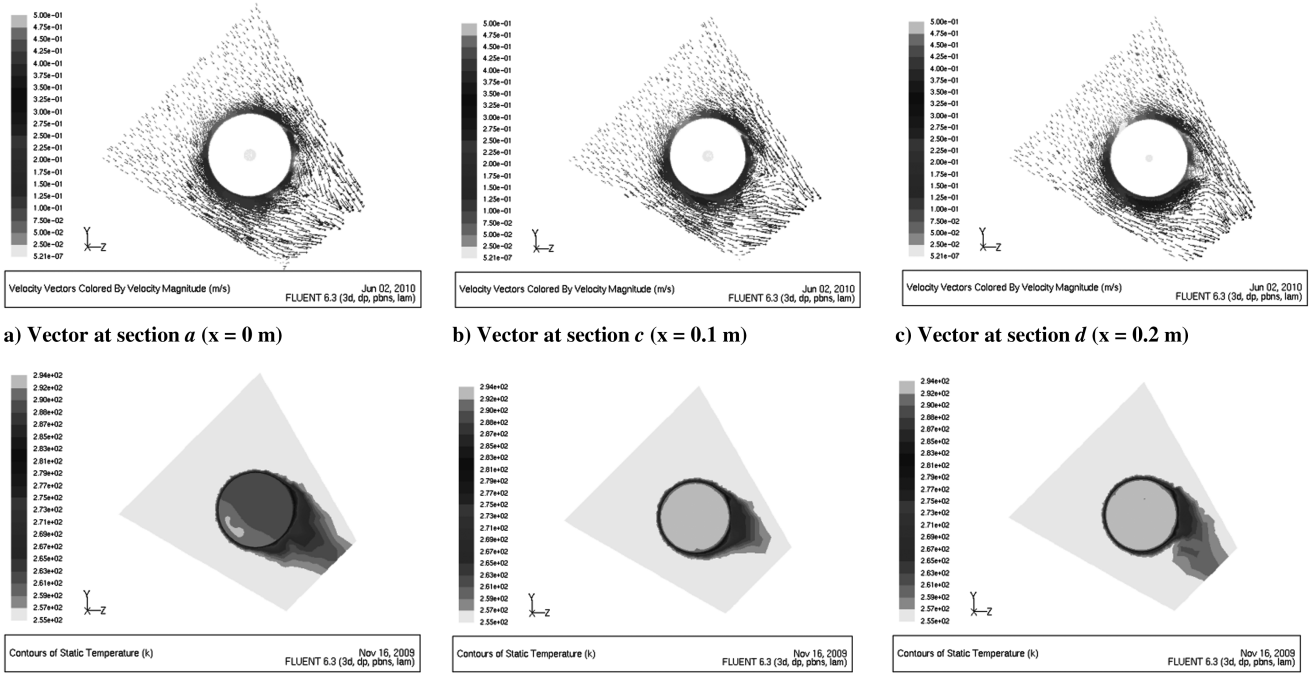

a) Vector at section *a* (x = 0 m) **b) Vector at section *c* (x = 0.1 m)** **c) Vector at section *d* (x = 0.2 m)**

d) Temperature at section *a* (x = 0 m) **e) Temperature at section *c* (x = 0.1 m)** **f) Temperature at section *d* (x = 0.2 m)**

Fig. 5 Flow patterns and temperature distributions of cooling air at various sections in steady-state case 1.

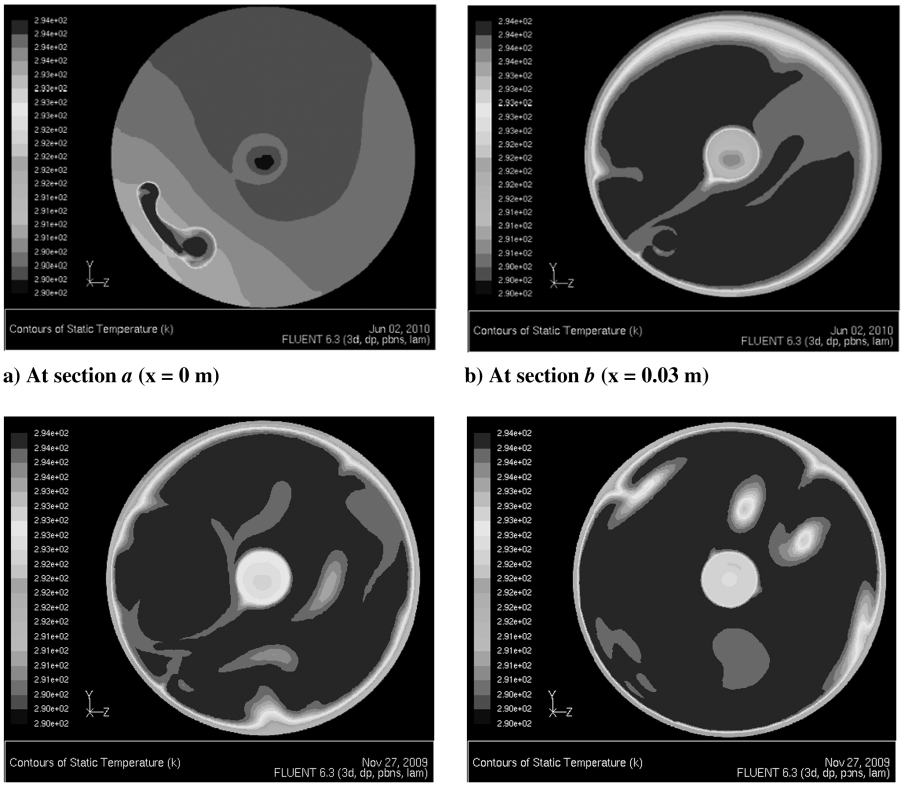

a) At section *a* (x = 0 m) **b) At section *b* (x = 0.03 m)**

c) At section *c* (x = 0.1 m) **d) At section *d* (x = 0.2 m)**

Fig. 6 Temperature distributions at the strategic cross sections in case 1.

be $C = 0.26$, $m = 0.6$, and $n = 0.36$, respectively [18]. Accordingly, $\bar{h}_c$ equals 2.22 W/m^2 k, and consequently, the heat transferred to the air is about 22.3 W for the length of 0.356 m of the cylindrical body. Comparing with the simulation result of 28.6 W for the heat transfer from the outer cylindrical lateral wall of the reservoir to the air, it can be seen that the results obtained both from the experimental correlation and the CFD simulation are very close. Considering many simplifications in the estimation of heat transfer using the Zukauakas correlation were taken, it is reasonable to consider the simulation result more closely coincides with the practical situation.

B. Steady-State Case 2

When inlet temperature of the working fluid is maintained at 394.3 K, the cooling air flow pattern and temperature distribution are different from the ones in case 1, as shown in Fig. 9. At the same time the working fluid also largely changes its flow pattern and temperature distribution, as shown in Fig. 10. Obviously, the fluid convection at the both sides of the reservoir wall is greatly strengthened, mainly by buoyancy effects. As a result, the temperature distributions at the sections *a*, *b*, *c*, and *d* show quite different characteristics from those in case 1, as seen in Fig. 11. Comparing Figs. 6 and 11, it can be seen that at section *a*, most portions of the lowest temperature region is replaced by higher temperature regions, while at sections *b*, *c*, and *d*, the overwhelming majority of the highest temperature regions have become moderate temperature regions except at the working fluid entrance.

The total absorbed heat by the reservoir, including the inlet and outlet tubes, is 343.8 W, while the reservoir body itself absorbs 288.8 W of heat, accounting for 84.0% of the total absorbed heat. The increase of percentage of the absorbed heat in the reservoir body, from 60.7 to 84%, is attributed to the enhanced buoyancy effects both in the working fluid and in the cooling air. It is expected that the higher the working fluid temperature, the higher percentage of heat is absorbed by the reservoir body.

It is interesting to note that the heat absorbed by the portion of the cylindrical side wall directly contacting the working fluid is 161.4 W, while the total heat transfer into the air through the whole cylindrical

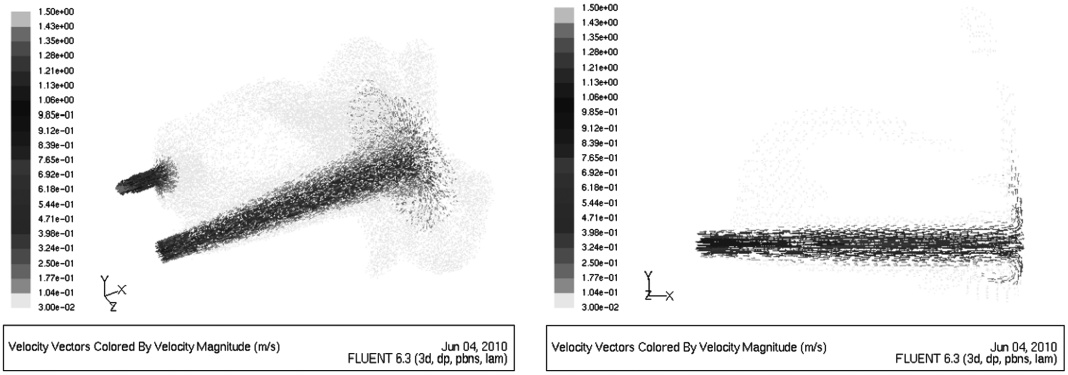

a) Fluid entrance jet and outflow stream **b) At the section of z = -0.052 m**

Fig. 7 Velocity vectors of working fluid in the reservoir in case 1.

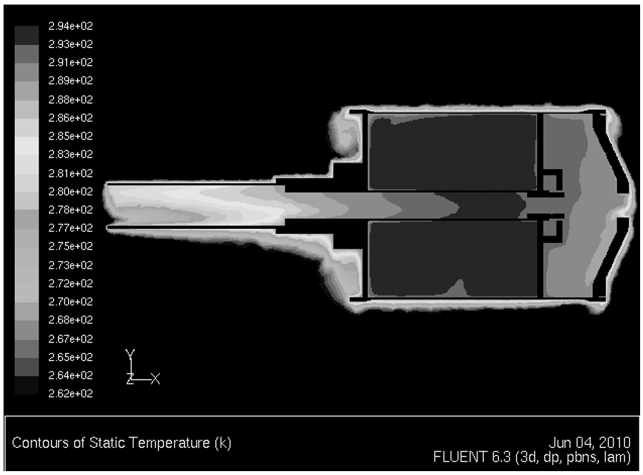

Fig. 8 Temperature distributions of the working fluid and the cooling air at the section of $z = 0$ m in case 1.

side wall is only 154.8 W. It indicates that more heat is transferred to the front cover assembly and piston through heat conduction and then transferred to the cooling air. Only 53.6% of the absorbed heat by the reservoir body is transferred to the cooling air through the cylindrical side wall, while 46.4% of the heat is transferred to the cooling air through the front cover assembly, the back cover assembly, and the central air channel. In other words, the percentage of heat transfer through the cylindrical side wall greatly decreases while more of the heat is transferred through the front and back cover assemblies and the central air channel when the working fluid temperature increases. Obviously, these heat transfer characteristics are quite different from those in case 1.

C. Transient Case

A simulation of a transient case was performed to obtain information on the total absorbed heat by the reservoir (including inlet and outlet tubes) when the flow inlet temperature is ramped from 294.3 to 352.2 K (70 to 174.3 F) over 4.63 min at the flow rate of 1.3880×10^{-4} m^3/s (2.2 GPM).

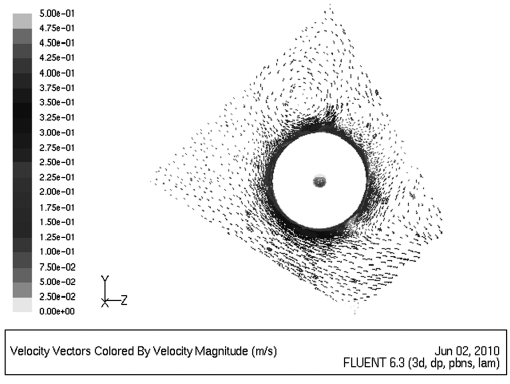

a) Vector at section *a* (x = 0 m)

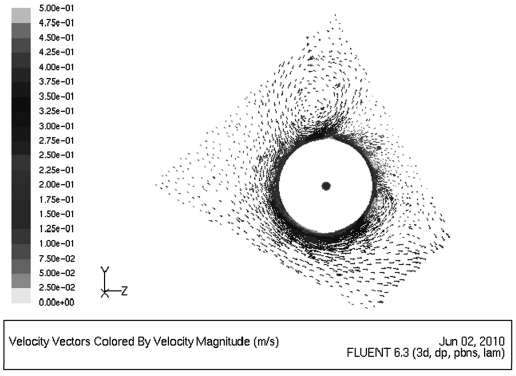

b) Vector at section *d* (x = 0.2 m)

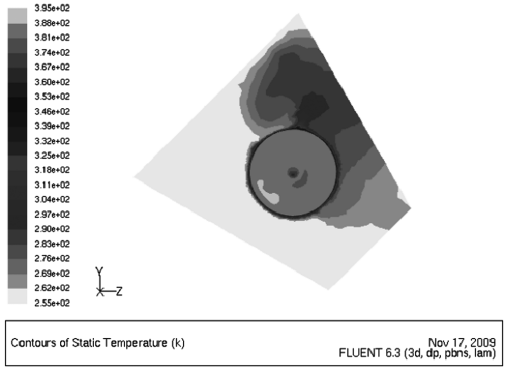

c) Temperature at section *a* (x = 0 m)

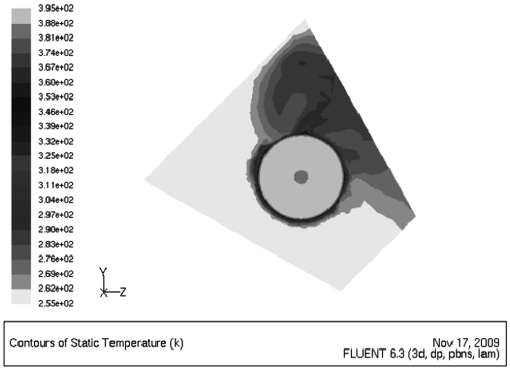

d) Temperature at section d (x = 0.2 m)

Fig. 9 Flow patterns and temperature distributions of cooling air in case 2.

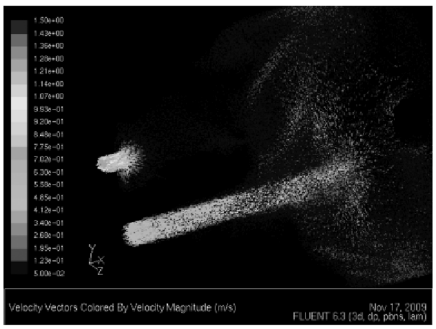

a) Velocity vectors

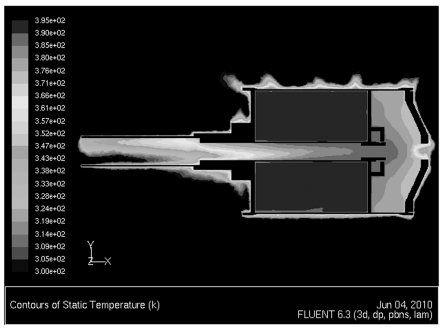

b) Temperature at section z = 0

Fig. 10 Velocity vectors of working fluid and temperature distribution at the section $z = 0$ in case 2.

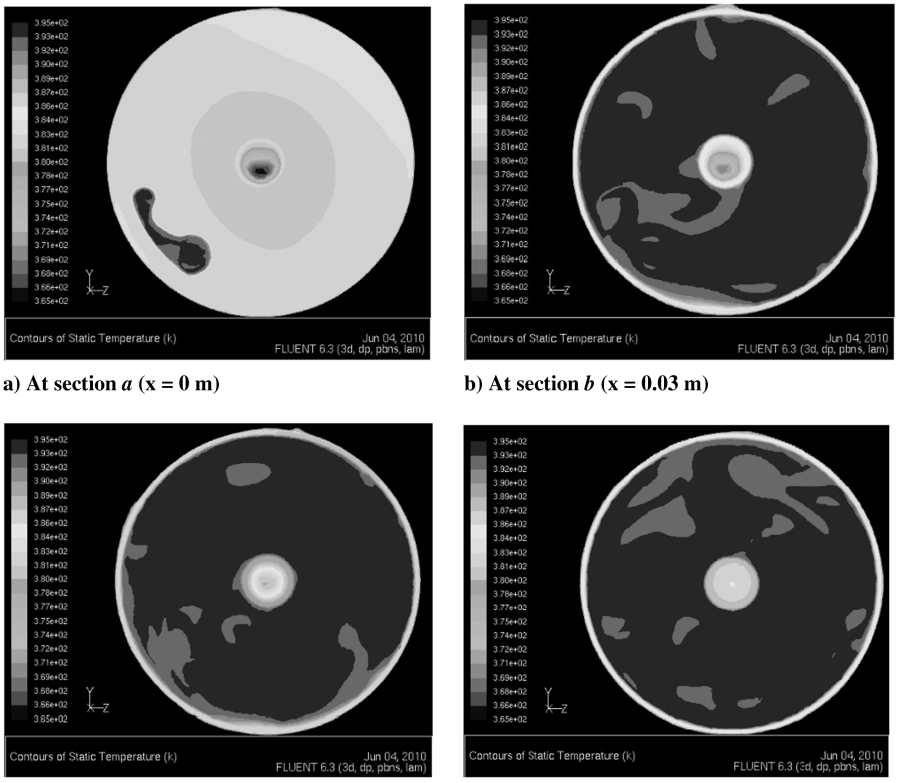

a) At section *a* (x = 0 m) **b) At section *b* (x = 0.03 m)**

c) At section *c* (x = 0.1 m) **d) At section *d* (x = 0.2 m)**

Fig. 11 Temperature distributions at the strategic cross sections in case 2.

The simulation started from the converged steady-state case 1 and ended when the inlet temperature reached 352.2 K at a flow time of 278 s. During this transient process, the buoyancy effects continually increase. Consequently, the flow patterns of the working fluid and the cooling air as well as the heat transfer performance were changing from those in the steady-state case 1 towards those in the steady-state case 2.

The convergence history of the working fluid enthalpy shows that the inlet mass-weighted average enthalpy increases linearly with time during the whole process, while the outlet mass-weighted average enthalpy does not change for the first 8 s and then nonlinearly increases until about 90 s, as shown in Fig. 12. After 90 s, the outlet enthalpy increase becomes almost linear. The total absorbed heat during this process can be calculated by

$$\Delta H = \int_0^8 \dot{m}(h_{f,\text{in}} - h_{f,\text{out}})\,\mathrm{d}t + \int_8^{90} \dot{m}(h_{f,\text{in}} - h_{f,\text{out}})\,\mathrm{d}t + \int_{90}^{278} \dot{m}(h_{f,\text{in}} - h_{f,\text{out}})\,\mathrm{d}t \tag{10}$$

The fluid enthalpy at the inlet over the entire flow time range of 0 to 278 s can be expressed as

$$h_{f,\text{in}} = -7798.9 + 437.617t \tag{11}$$

while the fluid enthalpy at the outlet can be expressed by three formulas:

$$h_{f,\text{out},1} = -8365.4 \quad \text{for } 0\text{ s} \le t < 8\text{ s} \tag{12}$$

$$h_{f,\text{out},2} = -9081.130 + 74.5365t + 595.6884 \times 10^{-3}t^2 + 8.6709 \times 10^{-3}t^3 \quad \text{for } 8\text{ s} \le t < 90\text{ s} \tag{13}$$

$$h_{f,\text{out},2} = 8848.1 + 391.120t \quad \text{for } 90\text{ s} \le t \le 278\text{ s} \tag{14}$$

It should be noted that the working fluid is pumped into the reservoir at a constant volume rate, therefore, the mass flow rate changes with time as the density changes with temperature. The total enthalpy entering into the reservoir per second is $\dot{m}h_{f,\text{in}}$, which can be expressed as a linear equation of time within the flow time range of 0 to 278 s:

$$\dot{m}h_{f,\text{in}} = -909.742 + 49.335t \tag{15}$$

while the total enthalpy exiting from the reservoir per second can be expressed as

$$\dot{m}h_{f,\text{out},1} = -975.824 + 0.1569t \quad \text{for } 0\text{ s.} \le t < 8\text{ s} \tag{16}$$

$$\dot{m}h_{f,\text{out},2} = -1079.019 + 13.449t - 64.55 \times 10^{-3}t^2 + 1.9323 \times 10^{-3}t^3 \quad \text{for } 8\text{ s.} \le T < 90\text{ s} \tag{17}$$

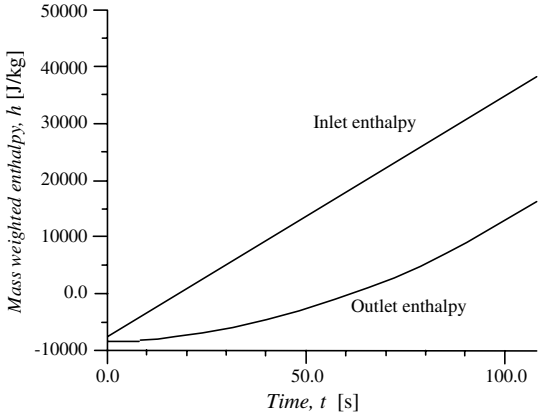

Fig. 12 History of mass-weighted enthalpies of the working fluid at inlet and outlet.

$$\dot{m}h_{f,\text{out},3} = -2682.516 + 41.108t \quad \text{for } 90 \text{ s.} \leq t \leq 278 \text{ s} \quad (18)$$

Upon substitution of Eqs. (15–18) in Eq. (10), it gives

$$\Delta H = 2.102 + 142.053 + 617.870 = 762.025 \text{ [kJ]} \quad (19)$$

IV. Discussion

CFD simulation was successfully applied to estimate and analyze the flow and heat transfer at both sides of the reservoir walls. It reveals that for different inlet temperatures of the working fluid, the flow convection patterns and heat transfer performances at both sides of the reservoir walls are dissimilar for the various effects of buoyancy. The simulation can also provide the individual amounts of heat transferred through various assemblies, and consequently, estimate the percentages of heat transferred through the individual portions of the reservoir.

When the reservoir is filled partially, say 75% full of working fluid, a particular heat transfer phenomenon may occur in the detained air chamber; the heat is transferred from the detained air to the reservoir wall in the top portion while from the reservoir wall to the detained air in the bottom portion, as described in the steady-state case 1.

As for the special transient case of inlet temperature ramping from a given temperature to another given temperature over a certain time period, the simulation can also provide the relevant parameter history and then estimate the accumulated amount of the parameters through integrations.

None of these unique functions can be realized by either calculations using empirical relations or experimental tests.

V. Conclusions

For the laminar flows, when inlet temperature of the working fluid is maintained at a low level, say 294.3 K, the buoyancy effects at both sides of the reservoir walls are not dominant in the flows. However, at a higher inlet temperature of the working fluid, say 394.3 K, this greatly changes both flow patterns and heat transfer performance of the working fluid and the cooling air around the reservoir due to the stronger buoyancy effects.

For the case of lower inlet temperature of the working fluid, greater amount of the absorbed heat by the reservoir is transferred through the cylindrical side wall, while for the case of higher inlet temperature of the working fluid, the percentage of the absorbed heat transferred through the cylindrical side wall of the reservoir greatly decreases, while a larger portion of heat is transferred through the front and back cover assemblies and the central air channel.

For the transient case of the inlet temperature of the working fluid ramping from 294.3 to 352.2 K over 278 s at the flow rate of 1.3880×10^{-4} m^3/s, the mass-weighted average enthalpy of the working fluid at the inlet increases linearly during the whole process, while at the outlet the working fluid mass-weighted average enthalpy does not change in the first 8 s, then nonlinearly increases until 90 s. After 90 s, the increase becomes linear. The total accumulated heat transferred into the cooling air can be calculated through the sum of the enthalpy difference integrations over the three time intervals.

References

[1] "NASA's Ares 1 Upper Stage, Powering the Second Phase of Rocket's Journey to Space," http://www.nasa.gov/pdf/231430main_UpperStage_FS_final.pdf [retrieved 8 Dec. 2009].

[2] "Thrust Vector Control," http://exploration.grc.nasa.gov/LaunchSystems/UpperStage/Thrust [retrieved 8 Dec. 2009].

[3] Pham, N. T., and Frate, D. T., "Initial Prototype of Ares 1 Upper Stage Thrust Vector Control and Associated One-Axis Test Rig Developed," http://ntrs.nasa.gov/archive/nasa/casi.ntrs.nasa.gov/20090021995_2009021568.pdf [retrieved 8 Dec. 2009].

[4] Dorfman, A., and Renner, Z., "Conjugate Problems in Convective Heat Transfer: Review," *Mathematical Problems in Engineering*, Vol. 2009, 2009, Article 927350.

[5] Kuo, J. C., and Lin, T. F., "Steady Conjugate Heat Transfer in Fully Developed Laminar Pipe Flows," *Journal of Thermophysics and Heat Transfer*, Vol. 2, No. 3, 1988, pp. 281–283. doi:10.2514/3.63065

[6] Ahmad, R. A., and Qureshi, Z. H., "Laminar Mixed Convection from a Uniform Heat Flux Horizontal Cylinder in a Crossflow," *Journal of Thermophysics and Heat Transfer*, Vol. 6, No. 2, 1992, pp. 277–287. doi:10.2514/3.356

[7] Ahmad, R. A., and Qureshi, Z. H., "Buoyancy Effects on Forced Convection from Horizontal Cylinder in a Crossflow," *Journal of Thermophysics and Heat Transfer*, Vol. 7, No. 4, 1993, pp. 574–580. doi:10.2514/3.463

[8] Chen, C.-K., Yang, Y.-Z., and Wu, S.-R., "Laminar Mixed Convection from a Circular Cylinder Using a Body-Fitted Coordinate System," *Journal of Thermophysics and Heat Transfer*, Vol. 8, No. 4, 1994, pp. 695–701. doi:10.2514/3.600

[9] Kao, K.-H., and Liou, M.-S., "Application of Chimera/Unstructured Hybrid Grids for Conjugate Heat Transfer," *AIAA Journal*, Vol. 35, No. 9, 1997, pp. 1472–1478. doi:10.2514/2.270

[10] Amin, M. R., "Conjugate Forced Convection Heat Transfer in Tubes with Obstruction," *Journal of Thermophysics and Heat Transfer*, Vol. 12, No. 1, 1998, pp. 114–116. doi:10.2514/2.6311

[11] Cole, K. D., and Beck, J. V., "Conjugate Heat Transfer from a Strip Heater with the Unsteady Surface Element Method," *Journal of Thermophysics and Heat Transfer*, Vol. 1, No. 4, 1986, pp. 348–354.

[12] Liang, P. W., and Cole, K. D., "Transient Conjugate Heat Transfer from a Rectangular Hot Film," *Journal of Thermophysics and Heat Transfer*, Vol. 6, No. 2, 1992, pp. 349–355. doi:10.2514/3.366

[13] Amon, C. H., "Spectral Element-Fourier Method for Unsteady Conjugate Heat Transfer in Complex Geometry Flows," *Journal of Thermophysics and Heat Transfer*, Vol. 9, No. 2, 1995, pp. 247–253. doi:10.2514/3.653

[14] Wang, T.-S., Luong, V., Foote, J., and Litchford, R., "Analysis of a Cylindrical Specimen Heated by an Impinging Hot Hydrogen Jet," Ninth AIAA/ASME Joint Thermophysics and Heat Transfer Conference, AIAA Paper 2006-2926, San Francisco, CA, 2006.

[15] Rehman, F., "Transient Conjugate Heat Transfer Analysis of a Turbine Stage using CFD," Ninth AIAA/ASME Joint Thermophysics and Heat Transfer Conference, AIAA Paper 2006-3264, San Francisco, CA, 2006.

[16] "Aerospace Hydraulic Fluids Physical Properties," http://www.sae.org/technical/standards/AIR1362B [retrieved 8 Dec. 2009].

[17] Raznjevič, K., *Handbook of Thermodynamic Table and Charts*, McGraw–Hill, New York, 1976.

[18] Kreith, F., and Bohn, M. S., *Principles of Heat Transfer*, 4th ed., Harper and Row, New York, 1986, pp. 348–356.